Multi-blade monolithic Euler springs with optimised stress distribution

J.V. van Heijningen[1,†], J. Winterflood[1] and L. Ju[1]
[1] OzGrav-UWA node, University of Western Australia, 35 Stirling Hwy, Crawley WA 6009, Australia
E-mail: [†]joris.vanheijningen@uclouvain.be

Abstract. Euler springs are used for vertical suspension and vibration isolation as they provide a large static supporting force with low spring-rate and use minimal spring material. To date multiple single-width, vertically-stacked, rectangular blades of uniform thickness have been used in the post buckled state, with half of the number buckling in each of opposing directions. This structure requires clamping the ends of the blades giving stick-slip problems. In this study we investigate the benefits of forming multiple, oppositely buckling blades, side- by-side from a single monolithic sheet of spring material. We investigate how to distribute the stress evenly along the length of the blade by contouring its width, as well as finding the optimal joining contour to distribute the stress evenly around the tearing joints between oppositely bending blades.

Keywords: Gravitational waves, Vibration isolation, Euler springs, Seismic noise

Introduction

With the first detection of gravitational waves (GWs) [1], we as mankind have made our most precise distance measurement to date. The first coincidence measurement of GWs with electromagnetic counterparts, GW170817, from a binary neutron star merger [2, 3] has provided a firm basis for the newly founded field of multi-messenger gravitational wave astronomy.

All these monumental measurements would not have been possible without decoupling the test masses of the detectors from the Earth's ever-present seismic motion. Vibration isolation systems are used in all GW detectors. Isolated objects approximate the notion of a freely falling (test) mass in the axis of interest for GW detection, i.e. the direction in line with main laser beam. However the multi-kilometre extent of the laser cavities and finite radius of the earth means that the gravitational pull on the test masses at each end is not perpendicular to the cavity, but acts on a slight angle (a fraction of a mrad) to the sensing axis. This angle, together with construction tolerances (which couple vertical-to-horizontal motion) mean that vertical vibration isolation has been almost as critical as horizontal isolation in all GW detection efforts.

The measurement sensitivity at the test mass exceeds that of any available sensor, so the last stages of vibration isolation necessarily consist of passive mechanical spring- mass stages cascaded one after the other to achieve the required isolation. Various styles of spring-mass structures have been developed for the Gingin High Power Optical Test Facility [4, 5], operated by the University of Western Australia (UWA), Advanced Virgo [6] and KAGRA [7]. Vertical vibration isolation is achieved in Advanced Virgo with horizontal cantilever springs with some magnetic non-linearity added to provide some anti-spring [8] around the operating region to lower the resonance frequency. In KAGRA, building on the experience of TAMA300 [10], Geometric Anti-Spring (GAS) [9] structures are used. These also use cantilever springs, but set at an angle up from horizontal, with each cantilever compressed longitudinally against a partner with mirror or radial symmetry, to achieve some non-linear snap-through effect which lowers the resonance frequency around the operating region.

Both of these approaches have a large amount of vertical suspension energy (*mgdh* of initial deflection *h*) stored in the spring material which necessitates a large spring mass commensurate with the energy stored. The GAS structure even has a significant fraction of additional stored energy in the longitudinal compression which acts as an anti-spring to cancel most of the normal spring coefficient. By contrast the UWA isolators employ Euler springs [11] which store no energy until loaded with sufficient weight to cause them to buckle, after which they feature low stiffness and relatively high frequency internal modes (due to minimal mass) when operating in the post buckled state. Low stiffness is desirable as it determines the spring-mass resonance and thus the seismic filter cut-off frequency, while high frequency internal modes are desirable as these modes set the frequency above which the seismic filtering becomes ineffective.

Here we describe a novel design of the buckled column. Earlier we have shown [17] that the squareness of the knee in the force-displacement characteristic at the onset of buckling is extremely sensitive to the launching angle. The slightest tendency for the column to buckle out on one side in preference to the other

producing a very rounded knee with consequent detrimental high resonance frequency when operated near the buckling point. We have also shown [17] that when the launching angle at each end of the column are equally but oppositely offset—so that the unbuckled blade starts as a gentle ”S” shape, and the column has no preferred direction in which to buckle—then again the knee becomes square and the resonance frequency low.

This sensitivity to launching angle becomes particularly problematic when the ends of the columns or blades are clamped. The reason being that with uniform thickness blades, the regions of highest stress (necessarily a large fraction of yield) occur right where the blades launch from the clamps. The slightest stick-slip motion between the highly stressed blade surface and the relatively unstressed edge of the clamp produces a non-zero launching angle which spoils the squareness of the buckling knee. Many times we would find that the first buckling cycle had a square force- displacement characteristic, while subsequent cycles were badly rounded. Since the blade material was well below yield, we put this down to stick-slip motion between blade and clamping jaws at the launching point.

The obvious solution to this problem is to use monolithic rather than clamped boundaries at the ends of the blades. The best design would seem to be a step change in blade thickness at the launching point so that clamping would be done on a thick part with low levels of stress and no tendency to stick-slip. Producing a step change in thickness, while possible, presents difficulties when the best spring material comes ready in thin sheets, and the tolerances required for machining the thickness are very small. For this reason we decided to try slotting the face of a uniform thickness spring blade lengthwise—so that half of the blade material bows out in one direction while the other half bows in the opposite direction. The high stresses then occur at the ”tearing” joints where sections of the blade are bending in opposite directions, and the blade can be clamped some distance away from these joints, in an area where the stress is much reduced.

In addition to making the end boundaries of the Euler springs monolithic by slotting a single spring sheet to allow parallel side-by-side strips with opposing bends, we also decided to even out the stress distribution along each strip by contouring the width (not thickness) of each strip along its length and varying the shape of the tearing joint to even out the stress distribution in that region.

In section 1 we present our method to determine the optimal blade shape for which we calculate the theoretical stiffness in section 2. Subsequent finite element analysis on the impact of contouring on the nominal load and blade stress is described in section 3. Results of performance measurements of the design applied to a glassy metal sample are shown in section 4. We end with conclusions and future prospects.

1. Determining the optimal contoured Euler spring blade

When a constant width Euler spring, clamped at both ends, is longitudinally compressed until it buckles, it will take on the shape of an elastica. This shape, however, has an uneven stress distribution with maximum stress at the ends and midpoint [12]. In order to minimise the spring mass for a given load, the thin column or blade undergoing Euler buckling should have uniform stress distribution. If the thickness of the blade material is constant, then the material will be evenly stressed when it is bent to a constant radius—forming segments of circular arcs as shown in the edge view of Fig. 1.

In order to obtain constant radius of bend, the area moment of inertia should vary in direct proportion to the applied moment. Since points of inflection along the blade mark spots with zero moment, the line-of-action of the applied force must be a straight line through these points of inflection and the applied moment must be proportional to the distance of the blade from this line. Since the blade thickness is to be constant, the moment of inertia is proportional to the width, and so the width of the blade should be made directly proportional to its displacement when maximally buckled, from the line-of-action. This proportionality appears as the straight lines of a bow-tie shape in the end view of Fig. 1 where the width of the material is zero at the points of inflection and maximum at the points of maximum moment.

Since the constant radius curvature of the thin spring makes it part of a cylinder, and the profile cuts required are planes which cut this cylinder, it follows that the resulting shapes which appear projected in the profile view must be arcs of ellipses as shown in the profile view of Fig. 1. While an ellipse is the shape in projection, the curve does not remain an ellipse shape once the material has been flattened out. If a cylinder is cut at some angle with a plane and then unrolled, the shape of the cut edge is instead a sinusoid. In other words, the shape to be cut out of the flat material are segments of a sinusoid curve.

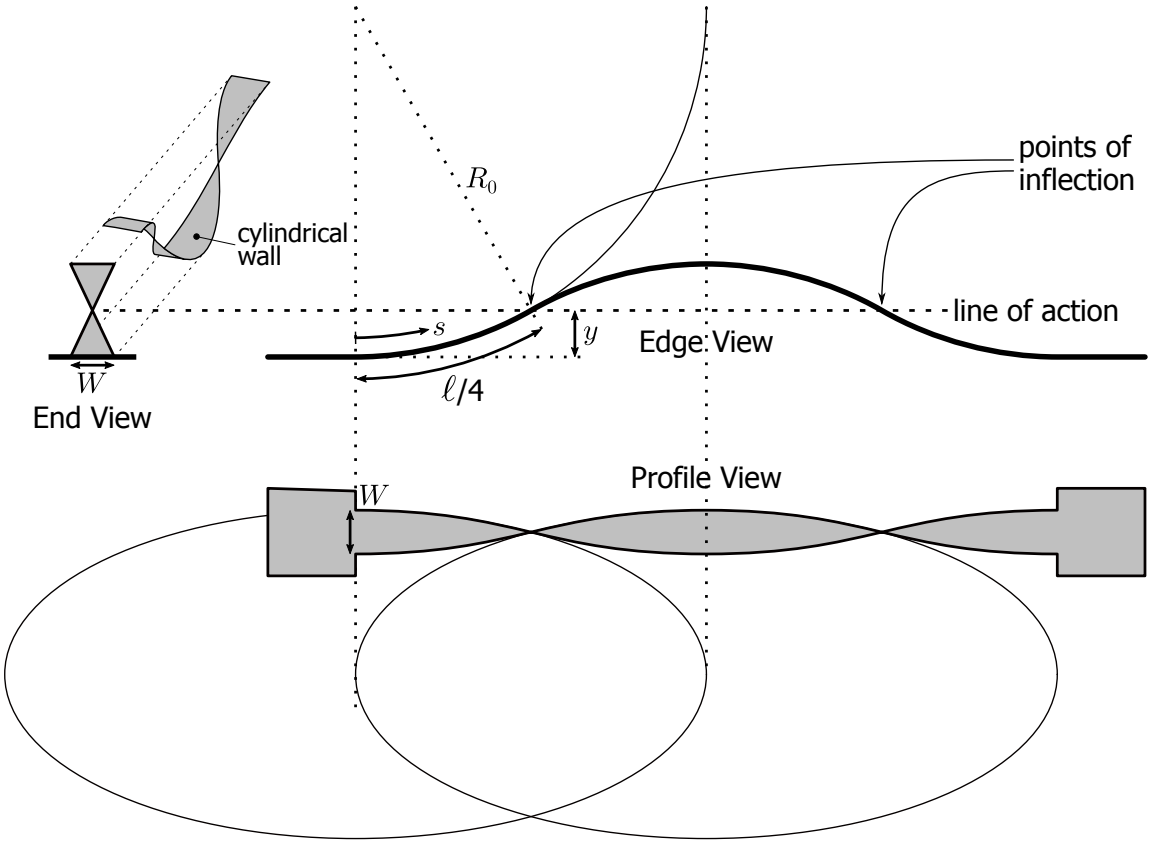

Figure 1. A width contoured Euler spring design. In the edge view we see the four quadrants of length $\ell/4$ drawn as arcs of circles of radius R. The profile view in buckled state features zero width points at the two points of inflection (PoIs), i.e. zero curvature transition points. The bow-tie end view shows how such a blade would look if one were to observe it along the axis of spring action.

Since such small segments of a complete ellipse or sinusoid are used, this curve is adequately approximated by either the arc of a circle (for CNC manufacturing) or a parabola (for mathematical analysis). The curve shape changes slightly depending on the degree of maximum buckling or minimum radius R_0 but with only slight-to- medium buckling (i.e. $R_0 \geq \ell/2$) and to first order in R_0/ℓ, the required width w of the blade varies with the distance s along it for the first quarter of its length ($0 \leq s \leq \ell/4$) as the simple parabola:

$$w(s) = W(1 - (4s/\ell)^2) \tag{1}$$

The remaining three quarters of the blade are simple symmetric reflections of this segment giving the overall shape shown as the profile view in Fig. 1. Of course the width of any practical blade would not go to zero at the inflection points, but rather have fillets to give some minimum width for robustness, and the parabolic curves would be manufactured as circular arcs without detriment.

2. The impact of the blade shape on Euler spring stiffness

Contrary to a rectangular spring which buckles to form an elastica, this blade shape will buckle to form circular arcs, and so it is quite straightforward to calculate the energy stored in the blade as a function of compression distance *x*. The force-displacement characteristic can then be obtained by differentiating the energy function, and the spring coefficient obtained from that. In the case of material with thickness t much less than its width (so that keystone deformation of its cross-section is insignificant) the stress and strain is a simple function of the radius of curvature *R* to which it is bent. With Young's modulus *Y* , the stress σ and strain ε peak at σ_0 and ε_0 at the surfaces of the material as

$$\epsilon_0 = \frac{t}{2R} \quad \text{and} \quad \sigma_0 = \frac{\mathrm{Yt}}{2\mathrm{R}}. \tag{2}$$

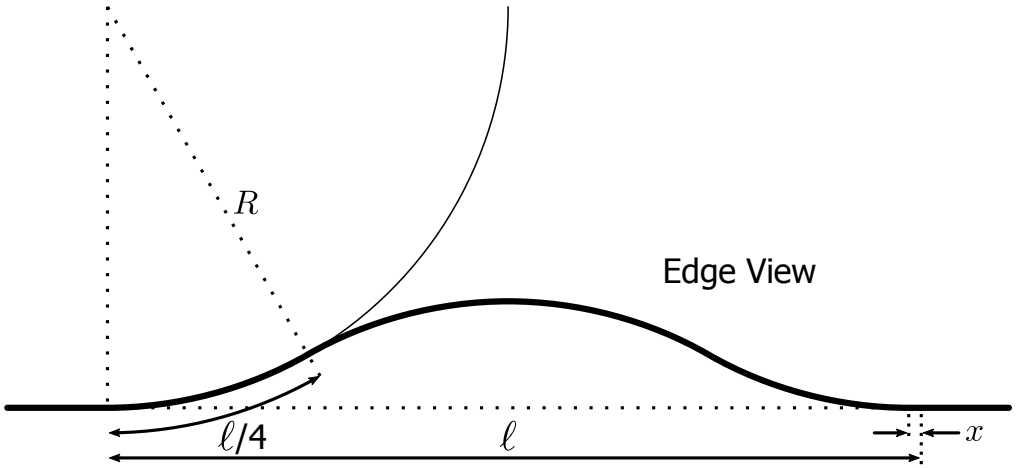

Figure 2. Edge view of a blade under compression with particular dimensions to aid in the derivations in the text.

The actual stress σ and strain ε vary from positive maximum at one surface to negative maximum at the opposite surface, linearly through the material. The integral of their product through the thickness gives the energy per unit of bent surface area. With the radius of curvature *R* being constant and the total surface area being obtained by integrating Eq. 1, we obtain an expression for the stored energy E_{st} as *energy per area* × *area*

$$E_{\mathrm{st}} = \frac{Yt^3}{24R^2} \times \frac{2}{3} W\ell = \frac{YI_a\ell}{3R^2} \tag{3}$$

, where I_{a} is the average area moment of inertia from the average width of the blade which is 2/3 of the maximum width *W*. From the geometry in Fig. 2, the relationship between compression distance *x* and radius of curvature *R* is

$$x = \ell - 4R \sin \frac{\ell}{4R}. \tag{4}$$

Obtaining an inverse series expression for R^2 in terms of *x*, substituting this into the stored energy expression (Eq. 3), and differentiating this expression to get the contoured Euler force F_{c} as a function of compression *x* gives

$$F_{\mathrm{c}} = \frac{32YI_{\mathrm{a}}}{\ell^2} + \frac{96YI_{\mathrm{a}}x}{5\ell^3} + \frac{2304YI_{\mathrm{a}}x^2}{175\ell^4} + \cdots \tag{5}$$

The first (constant) term gives the Euler buckling force, the second term (proportional to *x*) gives the initial spring coefficient, while the remaining terms indicate that the force-displacement relationship is slightly non-linear. It is of interest to compare this against the corresponding expression for a standard fixed-fixed rectangular Euler buckling spring

$$F_{\mathrm{r}} = \frac{4\pi^2 YI}{\ell^2} + \frac{2\pi^2 YIx}{\ell^3} + \frac{9\pi^2 YIx^2}{8\ell^4} + \cdots \tag{6}$$

If we compare contoured against rectangular blades of the same average width (ie same amount of spring material), then the force needed to buckle the contoured blade is ($8/\pi^2$ =) 81% of that required to buckle a rectangular blade. If we compare contoured against rectangular blades of the same maximum width, then the force needed to buckle the contoured blade is ((2/3) $8/\pi^2$ =) 54% of that required to buckle a rectangular blade.

We usually normalise the spring coefficient to the buckling force, and obtain a length value (in terms of the unbuckled length) to which a linear spring would need to be stretched in order to obtain the buckling force. Thus a linear spring would need to be stretched to twice the length of a rectangular blade to obtain a proportionate spring coefficient. For the case of the contoured blade this value reduces slightly to 5/3 or 1.67 times the length.

Considering the first non-linear spring coefficient term for its fractional change of spring rate with fractional extension indicates that the rectangular spring coefficient increases by 12.5% per spring length of displacement, while the contoured spring coefficient changes by 37% per spring length. Since we would like to maximise static force for minimal spring coefficient with minimal non-linearity, all of these changes are disadvantageous.

3. Practical blade design

The blade shape suggested in figure 1 gives the fundamental shape required to achieve an even stress distribution along the majority of the blade, but since lateral stability is required (to prevent sideways collapse into a "Z"shape) the blade width cannot be made very narrow at the points of inflection. The effective blade width at these points needs to be several times the blade thickness to ensure that it prefers to Z-bend out of the plane of the blade (i.e. in the buckling direction) rather than Z-bend in-plane. Our typical 3-legged test shapes had this ratio about 5 (4 mm total width for 0.75 mm thick).

Another design decision is the number of opposing blades to be implemented for this monolithic approach. Again lateral stability suggests as few blades as possible so they can be made wide in comparison to their thickness. Having only a single pair suggests that some residual torque may appear on the end clamps, and makes it difficult to pre-deflect the blades in the desired buckling directions in a simple manner. For these reasons we went with a symmetric three-legged design with the central blade having twice the width of the two outer blades.

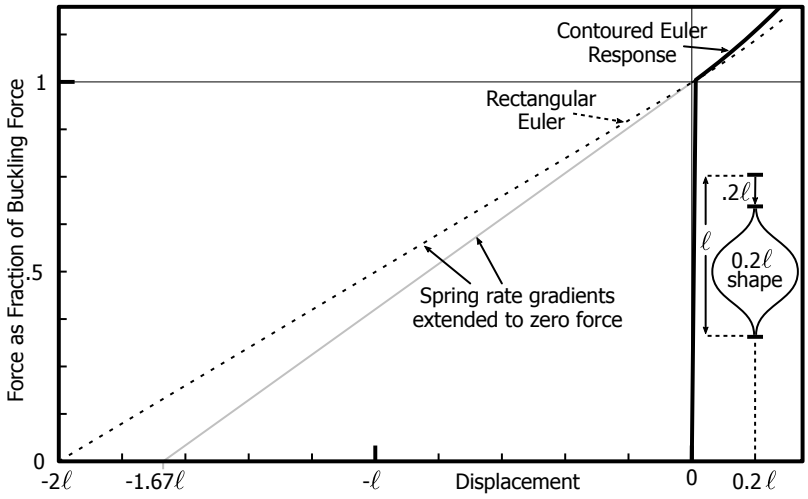

Figure 3. The force-displacement characteristic of the contoured Euler spring compared with a rectangular spring. The effective spring length is obtained by extending the initial force-displacement gradient from the buckling point to the zero force axis.

None of these considerations addresses the stress around the tearing joints between adjacent blades. It is clear that if the joint between legs ends is a sharp "V" shape, then stresses at the root of the V will exceed the main bending stresses (as evidenced by tearing before bending in weak rigid materials). If instead the tearing joint is a very wide "U" shape compared with the leg width, then the narrow legs must bend before there is any tendency to tear. However making the tearing joints wide and the legs narrow, means that the material in the legs providing the buckling force is very much reduced (having been removed to give wide "U" joints) so that the available force is very much reduced. Since the whole utility of the spring is the force that it provides, we need a compromise that gives as much force as possible for a given level of evenly distributed peak stress around the tearing joints. Since this optimisation is crucial and non-trivial, we engaged in an intensive finite element analysis investigation in an attempt to determine the optimum shape parameters.

Unlike rectangular Euler springs, here we aim to make the stress distribution as homogeneous as possible using finite element analysis in ANSYS. Fig. 4 shows the design of the blades used for the results presented in the rest of this paper. The shape of the Euler spring as shown in the figure were optimised for a maximum $F_{load}^2 / \sigma_{max}$.The above expression aims to optimise the desire for a high nominal load supported by the buckled blade while keeping the maximum stress as low as possible. A low maximum stress results from a highly homogeneous stress distribution. The maximum stress in these designs will always occur at the sharp bends between the individual blade close to the clamping surfaces of the springs (see example red dot in Fig. 4(a)). In that optimisation expression, we can chose to give weight to either the nominal load or the homogeneous stress by, for instance, raising F_{load} to a certain power *n.*

The numerical value n of the power in F^n/σ_{max} was determined by Finite Element Analysis (FEA) in ANSYS. Optimisation of the parameters shown in Fig. 5 is done by the FEA software maximising the ratio F^n/σ_{max} in each element of the simulated buckled spring. A spring is here 3 Euler blade shapes as in Fig. 1 attached at their respective ends. We not only optimise the width-to-length ratio of each single blade, but also the spline function that determined the shape of the cut between blades. Roughly speaking, the former optimises the nominal load, while the latter affects the maximum stress. A sharper bend will produce a higher stress and will spoil stress homogeneity.

Different values for n were used in the FEA assisted design optimisation, namely $0.5 < n < 4$ in steps of 0.25. Results of this analysis are shown in Fig. 6. Obviously, n determines the weight the blade designer assigns to the nominal load or low peak (von Mises) stress in the blade for a high or low value of n, respectively. As discussed above, increasing V1 will increase the nominal blade load. This will however reduce V2 and increase stress in that area, where the two adjacent blades buckle out of plane in opposite direction.

Fig. 6(a) shows how the nominal load increases when increasing the power n in the optimisation process. The maximum stress also increases shown in Fig. 6(b) as the single blade profile width increases and the spline curve (near the red dot in Fig. 4(a)) is sharper resulting in the stress distribution to become less and less homogeneous. A third order polynomial fit was performed to capture the overall trend in each plot.

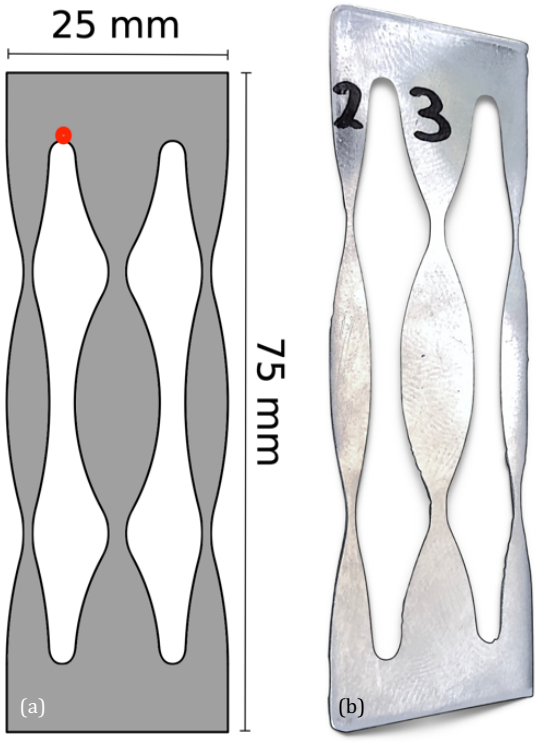

Figure 4. Panel (a) shows a three legged blade profile optimised by ANSYS for F^2/σ_{max}, i.e. maximum load squared homogeneous stress distribution load by demanding low maximum stress. Maximum stress occurs in the four points between the individual spring blades of which the red dot is one example. The dimensions were dictated by sample size of LM105 alloy blades acquired from Liquidmetal in March 2019. Panel (b) shows an edited photograph of this design with the numbers being there for our bookkeeping of version and number of the sample blade. Researcher fingerprints are clearly visible.

Fig. 6(c) shows the maximum load vs maximum stress, using the 3rd order polynomial fits of Fig. 6(a) and Fig. 6(b) (solid red lines). The red dot shows the values for $n = 2$ where we decided by eye the optimal value for n is, as further increasing n would only marginally increase load at an ever increasing price on the maximum stress.

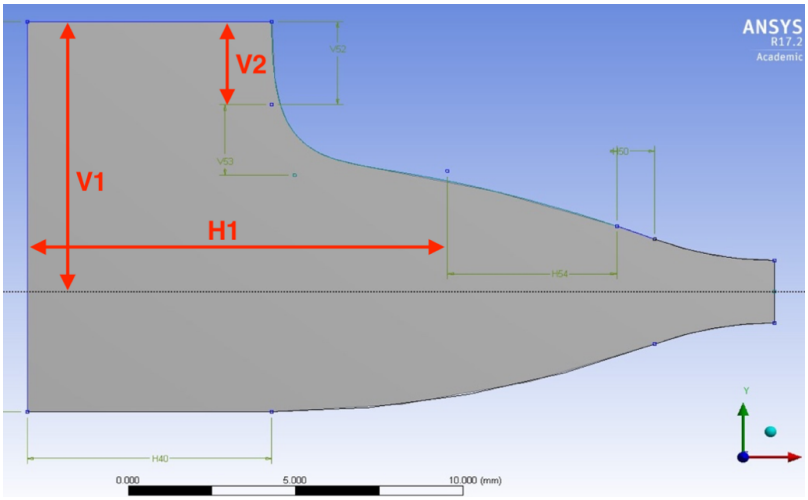

Figure 5. Blade design optimisation parameters for half of one corner of a blade. Found parameters are symmetrically observed at the 3 other corners. V1 determines the width of a blade and is the main driver for a high F_{load}. V2 and H1 determine the depth, shape and size of the spline function used to transition from the single blade profile of Fig. 1 to a vertical onset to the adjacent blade. The main driver for the shape is V2 and H1 determines the point at which the shape deviates from the elliptical single blade shape.

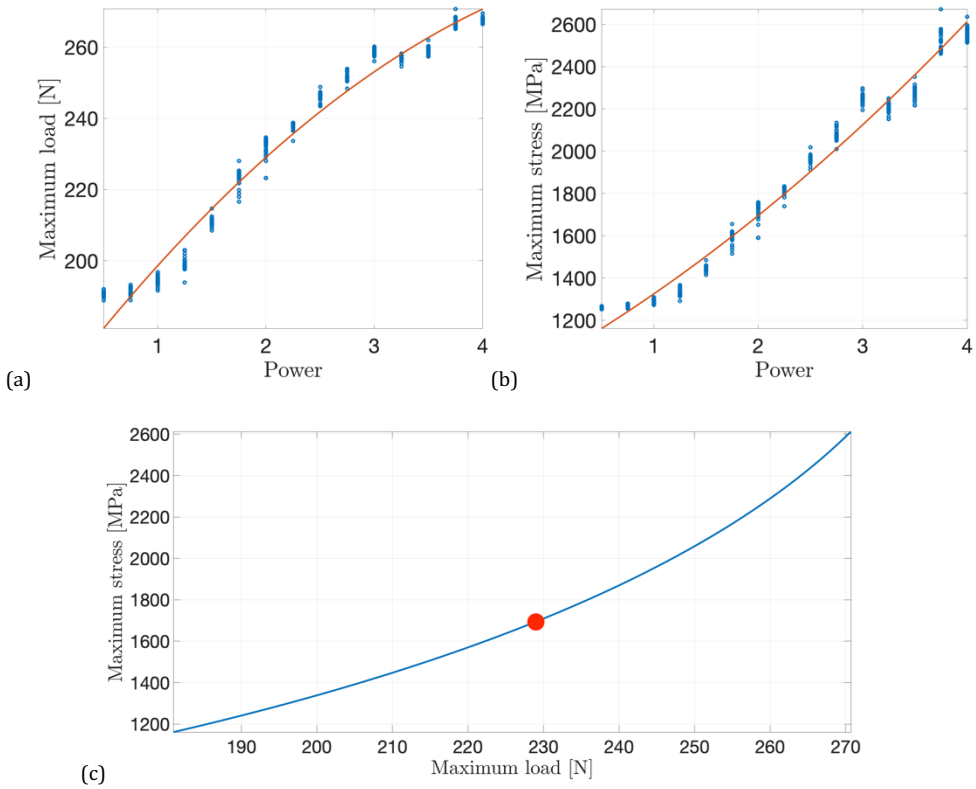

Figure 6. FEA optimisation results for (a) the blade's nominal load against the power n in F^n/σ_{max}, (b) the blade's maximum stress against the power n. Each blue dot is an iterative optimisation result. Variation is expected as calculation elements are of finite size and the maximum ratio is found through different paths in the meshed phase space. Both results are fitted with a simple third order polynomial fit to construct (c) the maximum stress against the load. The point of power n = 2 is shown by the red dot on the curve.

4. Stiffness measurement of glassy metal sample in a compression tester

An Instron 5982 compression tester was used to investigate the force versus displacement characteristic of the glassy metal sample blades. The spring stiffness over the operating range can be deduced from this test and will tell us how to set up the blade and what to expect in vibration isolation operation. In Fig. 7, the compression tester set-up is shown.One result of such compression test is shown in Fig. 8(a). The typical shape of a buckling spring is evident; the blade is compressed up to a certain $F_{\text{buck,c}}$ after which buckling commences. Further compression will generate a smaller reaction force per compressed distance. This slope is in fact the stiffness of the blade as shown in Fig 8(b).

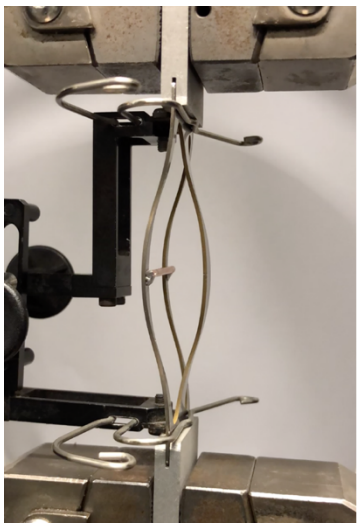

Figure 7. Still from analysis video of compression test of a glassy metal contoured Euler spring. Top and bottom show claws of tester with the compressed and buckled blade in between. A small cross bar is inserted between the three blades to assist in correct buckling direction. The extensometer to compare to the Instron's internal compression measurement is visible on the left. Full video found in ref. [13]. Cycles take about 20 seconds.

An estimate of the Q factor can be made by dividing the energy loss per cycle by the stored energy as

$$Q = 2\pi \frac{E_{\text{stored}}}{E_{\text{loss p.cycl.}}}. \qquad (7)$$

The stored energy can be determined by integrating the area below the compressing curve and the loss per cycle similarly by integrating the area between the releasing and compressing curve. The method assumes no difference, e.g. by thermo-elastic effects, between forced low frequency blade motion and higher frequency resonant motion. For measurements done on these blades Q factors between 1.2×10^4 and 1.7×10^4 were determined. The slope of the force against compression, shown in Fig. 8(b), is actually the stiffness of the blade, which we can calculate to be about 8.6 kN/m. This stiffness, combined with the mass load around 54 kgf of the

blade gives a potential resonance frequency of 2 Hz. The slope of about F_{buck}/ℓ is about a factor 1.7 smaller than theoretically calculated in section 1. At present, a reason for this discrepancy is uncertain. Speculatively, the material added at the inflection points and, probably to greater effect, the material added around the base of each blades, contributes to the stiffness.

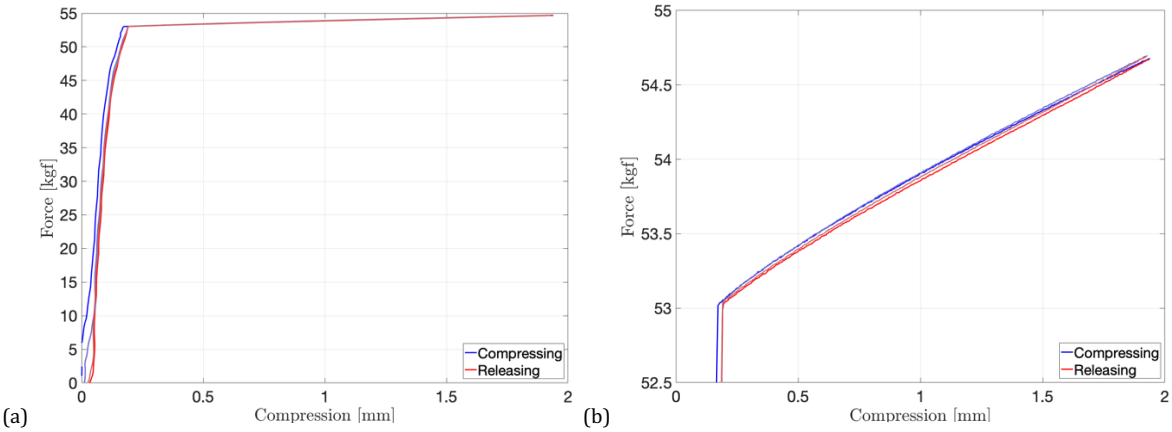

Figure 8. Compression test result of the first, fourth and ninth cycle of a 10- cycle-long measurement on a glassy metal monolithic contoured Euler spring. Panel (a) shows the typical buckling curve. The non-smooth rise towards the smooth buckling curve could be setting of the extensometer legs upon compression or real hysteric behavior of the material upon compression. Panel (b) zooms in on the spring behavior of the blade. The slope of the buckled blade that represents the stiffness of the spring is ill understood - its magnitude is about F_{buck}/ℓ

Conclusions and future prospects

We have presented a theoretical analysis of the ideal blade shape stemming from a desire to minimise blade material by shaping the blade contour such that stress was distributed with maximum homogeneity while maintaining decent spring performance. A triple blade monolithic design avoids issues with individual blade launch angle differences and residual torques at the base. The triple blade design has been analysed in ANSYS to optimise for certain dimensional parameters. A weighted optimisation of nominal load and maximum stress resulted in an optimised design. This design was cut out of glassy metal samples and tested in a compression tester.

The compression tester result shows typical Euler spring behaviour. Despite the post-buckling stiffness slope being higher than expected due to unknown reasons, the relatively high measured Q makes this vibration isolation solution an interesting candidate for future designs. The natural frequency of an Euler spring stage can be lowered by installing the springs under an angle with one side of each blade clamped to a central keystone from which high loads can be suspended. The overall resonance frequency can be lowered to arbitrarily low values this way, which will have a decreasing effect on the Q as well as the dynamic range of the system. A three Euler spring in a triangular formation is proposed. A trial with just two springs is first pursued [14]. These compact, high quality, future systems can be used for vibration isolation systems of future GW detectors, such as Einstein Telescope [15] or Cosmic Explorer [16]. Additionally, springs in such configuration can also be used in proof mass suspensions for low frequency, high quality, vertical inertial sensors.

Acknowledgements

This work was funded by the Australian Research Council (ARC) Centre of Excellence for Gravitational Wave Discovery OzGrav under grant CE170100004. We would like to thank Andrew Sunderland, Alessandro Bertolini, David Blair, Bram Slagmolen and Joshua McCann for useful discussions and comments. Additionally, we would like to acknowledge contributions from students Lindsay Wood and Wenjing Zheng early on. The authors also wish to thank the workshop technicians Ken Field and Steve Key.

References

[1] B.P. Abbott et al., "Observation of Gravitational Waves from a Binary Black Hole Merger", Phys. Rev. Lett., vol. 116, pp. 061102 (2016)

[2] B.P. Abbott et al., "GW170817: Observation of Gravitational Waves from a Binary Neutron Star Inspiral", Phys. Rev. Lett., vol. 119, pp. 161101 (2017)

[3] B.P. Abbott et al., "Multi-messenger Observations of a Binary Neutron Star Merger", ApJL, 484(2), L12 (2017)

[4] J. C. Dumas et al., "Testing of a multi-stage low-frequency isolator using Euler spring and self-damped pendulums", Class. Quant. Grav., 21(5), pp. S965–S971 (2004)

[5] E. Chin et al., "AIGO High Performance Compact Vibration Isolation System", Journal of Physics: Conference Series, 32, pp. 111–116 (2006)

[6] F. Acernese et al., "Advanced Virgo: a second-generation interferometric gravitational wave detector", Class. Quant. Grav. 32(2), pp 024001 (2014)

[7] T. Akutsu et al., "Construction of KAGRA: an Underground Gravitational Wave Observatory", Progress of Theoretical and Experimental Physics, Volume 2018, Issue 1, 013F01 (2018)

[8] M. Beccaria et al., "Extending the VIRGO gravitational wave detection band down to a few Hz: metal blade springs and magnetic antisprings", Nuc. Instrum. and Meth. A, Vol. 394, pp. 397–408 (1997)

[9] G. Cella et al., "Monolithic geometric anti-spring blades", Nucl. Instr. and Methods in Phys. A 540(2), pp. 502 - 519 (2005)

[10] S. Marka et al., "Anatomy of TAMA SAS seismic attenuation system," Class. Quant. Grav., vol. 19, pp. 1605–1614 (2002)

[11] J. Winterflood et al., "Using Euler buckling springs for vibration isolation", Class. Quant. Gravity 19(7), pp. 1639–1645 (2002)

[12] J. Winterflood et al., "High performance vibration isolation using springs in Euler column buckling mode", Phys. Lett. A, Vol. 300(2–3), pp. 122-130 (2002)

[13] Euler springs at UWA, YouTube (2019)

[14] J.J. McCann et al. "Suspensions and (rotational) accelerometers at OzGrav's UWA node", DCC number G1901603, LVK Autumn meeting (2019)

[15] M. Abernathy et al., " Design Report Update 2020 for the Einstein Telescope", Tech. Rep. ET-0007B-20, https://apps.et-gw.eu/tds/?content=3&r=17245 (2011)

[16] B.P.Abbotetal.,"Exploring the Sensitivity of Next Generation Gravitational Wave Detectors", Class. Quant. Grav. 34, pp. 044001 (2017)

[17] J. Winterflood, T.A. Barber and D.G. Blair, "Mathematical Analysis of an Euler Spring Vibration Isolator", Phys. Lett. A 300, Iss. 2–3 (2002)